JOURNAL OF GEOPHYSICAL RESEARCH, VOL. 112, B07401, doi:10.1029/2006JB004631, 2007

On the dynamics of a hydrous melt layer above the transition zone

Garrett M. Leahy[1] and David Bercovici[1]

Received 14 July 2006; revised 7 March 2007; accepted 4 April 2007; published 4 July 2007.

[1] The "transition zone water filter" (Bercovici and Karato, 2003) model relies on the presence of a dense hydrous melt above the 410-km discontinuity that is formed by dehydration melting as wet wadsleyite undergoes a phase change to low-water-solubility olivine. Recent studies suggest that, particularly in the Pacific, there is sufficient water in the transition zone for dehydration melting to occur. Here we construct a model for melt spreading and entrainment along the 410-km discontinuity. In particular, we propose a mechanism for melt entrainment in downwelling regimes at ambient mantle temperatures. We find: (1) that this entrainment mechanism is efficient in that it does not require melt to reach subducting slabs in order to recycle most of the upwelling water; (2) that in steady state, the efficiency of entrainment does not necessitate the existence of a thick melt layer; (3) that the entrainment of hydrous, buoyant material into the transition zone significantly affects the bulk mantle flow field, thereby diminishing entrainment efficiency and allowing the melt to spread further; (4) that these interactions help to recirculate water from the entrained regions through the transition zone; and (5) that the adjustments in bulk mantle velocity due to water entrainment are characterized by a broadening of upward flow with a corresponding decrease in amplitude. Our model predicts regions of high water content in the transition zone at ambient mantle temperatures, which may contribute to seismic observations of high attenuation near slabs.

Citation: Leahy, G. M., and D. Bercovici (2007), On the dynamics of a hydrous melt layer above the transition zone, *J. Geophys. Res.*, *112*, B07401, doi:10.1029/2006JB004631.

1. Introduction

[2] Recent mineralogical studies indicate that the transition zone (TZ) region of the deep upper mantle may be a substantial reservoir for water [e.g., *Kohlstedt et al.*, 1996; *Bolfan-Casanova et al.*, 2000]. In particular, these studies found that there is a large water solubility contrast between olivine (the drier, dominant upper mantle phase) and wadsleyite (the wetter, dominant TZ phase above 520 km). This implies that dehydration melting might occur as warm, even slightly hydrated material upwells across the 410-km discontinuity and changes from wadsleyite to olivine [e.g., *Inoue*, 1994; *Ohtani et al.*, 2000]. *Bercovici and Karato* [2003] hypothesized that melting above the TZ can act to decouple trace element circulation from bulk mantle flow, thereby satisfying the geochemical requirements for separate mid–ocean ridge basalt and ocean-island basalt source regions while maintaining whole mantle convection. Their "transition zone water-filter" (TZWF) model (Figure 1) predicts the presence of a dense, hydrous melt layer that spreads above the 410-km discontinuity.

[3] The initiation of melting at 410 km depth relies not only on the aforementioned solubility contrast but also on the water content of upwelling wadsleyite. Recent studies [*Huang et al.*, 2005, 2006] using electrical conductivity data from the Pacific Basin imply that the TZ water content is $\sim$0.1–0.2 wt%, exceeding the olivine solidus at ambient mantle temperatures and therefore allowing for the possibility of dehydration melting of ambient upwelling mantle material. The TZWF model also requires that the melt should be more dense than solid olivine (but lighter than solid wadsleyite) and should therefore collect above the 410-km boundary. *Ohtani et al.* [1995] postulated that the dry peridotitic melt should be more dense than the solid below 11–12 GPa. A recent study by *Matsukage et al.* [2005] suggested that for certain water contents, a hydrous silicate melt could be more dense than solid olivine at transition zone pressures. Other volatiles, for example K_2O [*Wang and Takahashi*, 2000] and CO_2 [*Dasgupta and Hirschmann*, 2006], could act to both enhance melting at the 410-km discontinuity and increase the density of the resulting silicate melt [*Karato et al.*, 2006].

[4] The role of dehydration melting at the 410-km discontinuity still remains controversial [*Hirschmann et al.*, 2005], especially when considering a realistic phase loop (the thickness of which depends on water and iron concentrations) and the effects of secondary phases (such as garnet). However, from a geodynamical perspective, the region where melt is potentially produced is reasonably simple. If the melt fraction is high enough that melt pockets are interconnected [*Karato et al.*, 2006], a dense melt would accumulate at its depth of neutral buoyancy in steady state and segregate from the solid [*Karato et al.*, 2006]. Of

[1]Department of Geology and Geophysics, Yale University, New Haven, Connecticut, USA.

0148-0227/07/2006JB004631$09.00

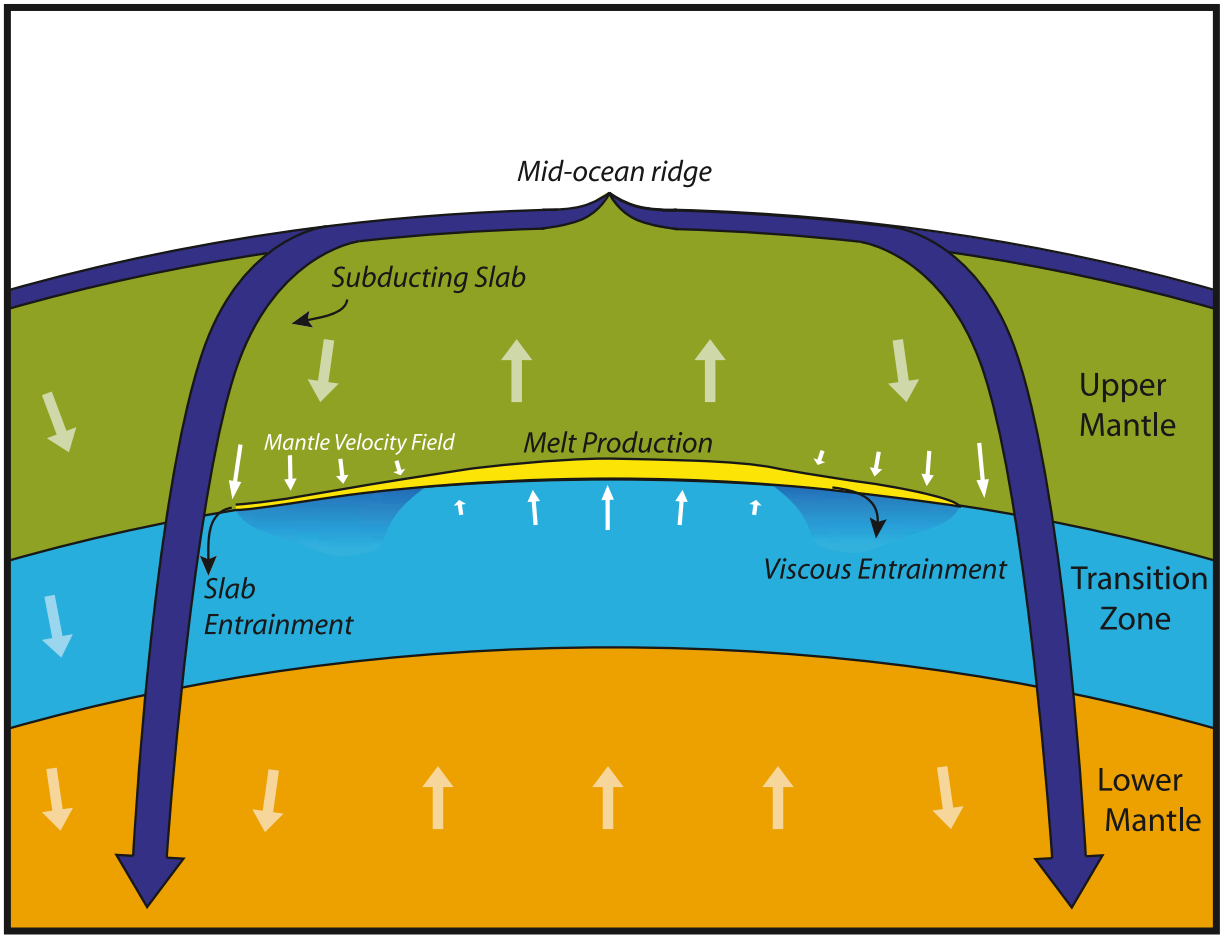

Figure 1. Schematic of the water-filter model: As upwelling mantle is hydrated in the transition zone and crosses the 410-km discontinuity, dehydration melting occurs. The dense melt spreads toward slabs, where it is eventually returned to the mantle.

more immediate concern is how melt and in particular volatiles such as water are returned to the TZ and lower mantle. If water is not recycled into the lower mantle, dehydration melting would eventually cease, and the TZWF model would be at best transient and would not be able to predict the steady state geochemical signatures of mantle reservoirs.

[5] In their model, *Bercovici and Karato* [2003] proposed a mechanism for melt (and water) recycling that relies on the effects of "cold" slab temperatures; in particular, when melt spreads near a cold slab, silicates crystallize out of the melt and are entrained downward. The entrainment of silicates partially dehydrates the melt layer, but an excess of water still remains. The excess water diffuses into the slab itself through the slab-melt contact surface. Bercovici and Karato's model allows the thickness of the melt layer (and therefore the area of slab-melt contact) to adjust until a steady state cycle of water and silicates is achieved.

[6] This model neglects two significant effects, in particular the interactions between a water-enriched melt layer and ambient mantle, and the fact that in order to arrive in the cold regions near slabs, the melt must traverse a large region of downward flow (where melt is not produced) at ambient mantle temperatures (Figure 2).

[7] Here we propose a geodynamical model for the structure of a dense, hydrous melt spreading at the 410-km discontinuity. In particular, we wish to address the fate and horizontal extent of the melt after it has been produced and spreads toward subducting slabs. We propose a new mechanism for melt entrainment at ambient mantle temperatures (before melt reaches the slab), which plays an important role in melt recycling: As melt is advected below the 410-km phase change, excess water is liberated, causing a melting reaction that allows the melt layer to spread horizontally. In steady state, the new entrainment mechanism is very efficient and does not necessitate a thick melt layer. This mechanism also results in heterogeneous water content in the TZ, leading to significant buoyancy anomalies that excite small-scale circulation, which in turn may help to redistribute entrained water in the TZ. We also find that these flow perturbations impede melt entrainment and allow melt to spread further than when the buoyancy anomalies are neglected. This model predicts high-water-content structures in the TZ that may account for features suggested in tomographic images and other seismic data. Geodynamical estimates of the horizontal extent of this putative melt layer are needed to test this model with seismic data and to

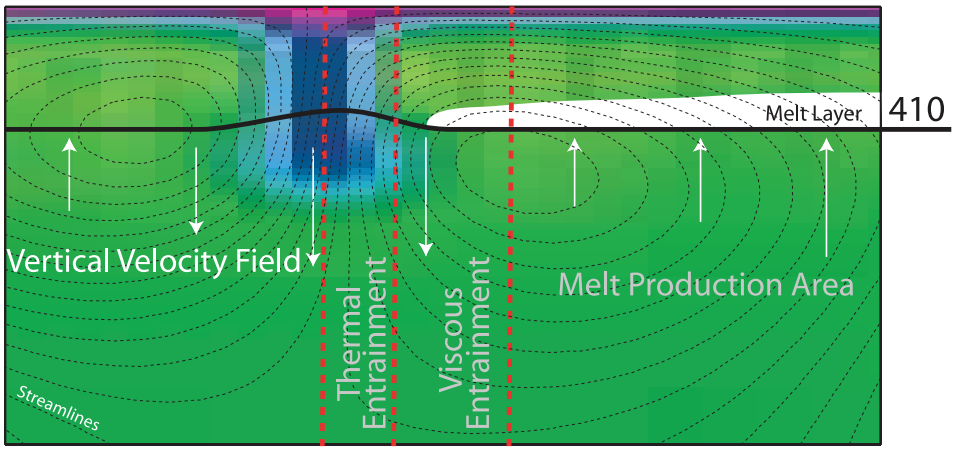

Figure 2. Possible melt regimes: A flow field from a convection simulation shows zones where melt may be produced by dehydration melting (MPZ), where melt is downwardly entrained at ambient temperatures (VEZ) and where melt may be entrained by diffusion into the slab (TEZ). Blue regions represent colder temperatures, while green regions are at ambient mantle temperatures. Streamlines (black) indicate the slab-driven mantle flow field.

differentiate it from other upper mantle melting models [e.g., *Hirschmann et al.*, 2005; *Kawamoto et al.*, 1996].

2. Melt Layer Model

[8] In the model of *Bercovici and Karato* [2003], melt produced by upwelling mantle spreads laterally along the 410-km discontinuity until it contacts a downgoing slab. In this colder regime, water is lost from the melt primarily through silicate crystallization and lateral diffusion into the dry slab. However, this simple model is not adequate in a more realistic mantle flow field. While it is straightforward to consider melt spreading in upwelling regions where melt production results in an interconnected network of channels, there is a downwelling region (a slab-driven viscous boundary layer) at ambient mantle temperatures that the melt must traverse in order to reach the colder slab region (Figure 2). For clarity, we will refer to regions where melting occurs as melt production zones (MPZ), regions where melt is entrained at ambient temperatures as viscous entrainment zones (VEZ), and regions where melt is entrained at cold temperatures as thermal entrainment zones (TEZ). *Bercovici and Karato* [2003] model entrainment in the TEZ, whereas this paper addresses entrainment in the VEZ.

[9] For the purposes of our model, we will consider melting and melt entrainment at ambient temperatures between two parallel descending slabs. The MPZ is defined by the region of passive upwelling (to conserve mass) between the slabs, and the VEZ is the slab's viscous boundary layer.

[10] The model we propose is based on the phase equilibria of the olivine-wadsleyite-water system near the phase transition (schematic, Figure 3). Assuming a dry melting point of 2200°C, χ^e_{ol} = 15.0 wt% at 1600°C [*Litasov and Ohtani*, 2002], and $\chi^\star_{ol}$ = 0.1 wt% at $T_e \sim$ 1200°C [*Stalder et al.*, 2001], one can estimate the liquidus and solidus curves at ~14 GPa. We assume that at the 410-km discontinuity wadsleyite, melt, and olivine can coexist in equilibrium and that hydrous melting and crystallization can be described by batch processes. Melting occurs when wet wadsleyite undergoes a phase transition to olivine (with lower water solubility). As long as the water content in the wadsleyite χ_{wd} exceeds the olivine solidus water content χ^s_{ol} (Figure 3a), partial melting will occur (model parameters are defined in Table 1 for reference). The fraction of melting is given by the lever rule:

$$\mathcal{F} = \left(\frac{\chi_{wd} - \chi^s_{ol}}{\chi^l_{ol} - \chi^s_{ol}} \right) \tag{1}$$

[11] The water content of the resulting melt is the olivine liquidus χ^l_{ol} value. The melt is in equilibrium with residual olivine of solidus water content χ^s_{ol}. Because recent evidence suggests that a hydrous silicate melt has a low dihedral angle at transition zone T, P [*Yoshino et al.*, 2007], it is likely that the dense melt drains from the bulk solid and collects above the 410-km discontinuity [*Karato et al.*, 2006] although this could be complicated by a decrease in permeability due to extreme wetting. Because of this draining and melt accumulation, it is reasonable to treat the melt layer as a homogeneous fluid surrounded by a high viscosity medium rather than a two-phase melt and matrix. This approximation permits us to model the melt layer as a gravity current collapsing under its own weight, supplied by a source of fresh melt along its base (Figure 4). For simplicity, we assume that the phase transition at the 410-km discontinuity is infinitely sharp and that the interface is flat and isothermal (which is a reasonable assumption far from slabs and plumes). Thus our model consists of a two-dimensional gravity current on a flat interface.

[12] The assumption that melt spreads along a relatively flat interface is consistent with the assumption that the melt density is intermediate to that of olivine (lighter) and wadsleyite (heavier). The depth in the mantle at which the melt spreads is, however, more likely its depth of neutral buoyancy. When considering a finite thickness phase loop (due to iron or water content) for the wadsleyite to olivine phase transformation, the melt's depth of neutral buoyancy would lie somewhere in the loop instead of on top of it. We loosely refer to this depth as the 410-km discontinuity because this is where we would expect the largest discon-

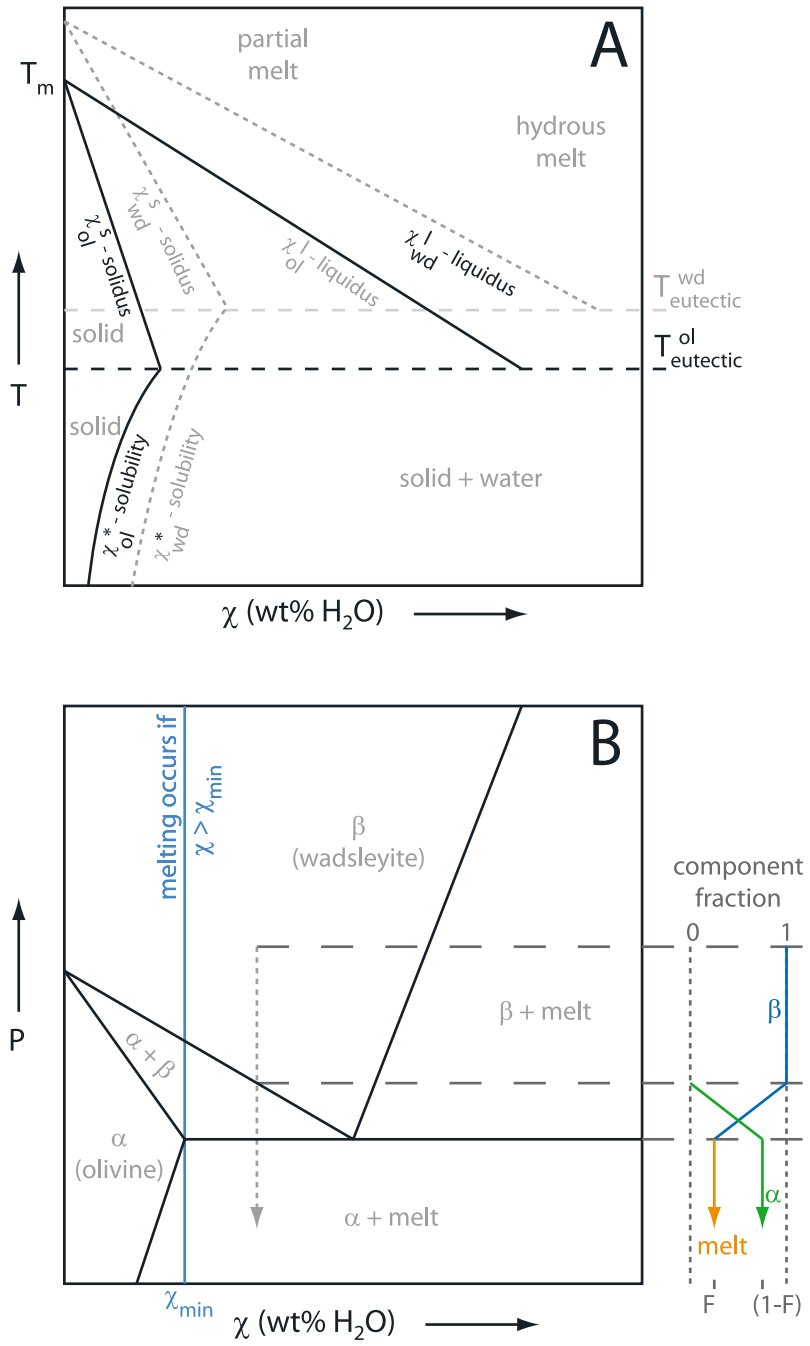

Figure 3. Schematic phase diagrams for olivine-wadsleyite-water systems. (a) Temperature versus weight percent H_2O eutectic schematic phase diagram for the olivine-water (solid, black) and wadsleyite-water (gray-dashed) system at a given pressure. Below the eutectic T_e, the solid is in equilibrium with free water when the water content exceeds the saturation value $\chi^\star$. Above T_e, the system can fall into one of three categories: hydrated solid (far left), pure melt (far right), or partial melt (center) where the melt fraction $\mathcal{F}$ is given by equation (1). B) Pressure versus weight percent H_2O schematic phase diagram for the olivine-wadsleyite-water system at a given temperature. Melting occurs when the transition zone water content exceeds χ_{min}. The side panel diagrams mass fractions of melt, olivine, and wadsleyite when hydrated wadsleyite rises (decompresses) from the transition zone. The phase fraction of olivine and wadsleyite in the loop is given by the lever rule, and similarly, the final melt fraction $\mathcal{F}$ is given by equation (1).

tinuity in seismic velocities and, for simplicity, neglect the existence of the phase loop in the model.

[13] An example of how melt is produced during decompression through the phase loop can be illustrated via the schematic in Figure 3b. Following the dotted path, wet wadsleyite ascends until it reaches the top of the olivine/wadsleyite phase loop. Then it begins to transform into olivine until both the olivine and the wadsleyite reach their

Table 1. Model Parameters

Symbol	Description	Earth Value
$\mathcal{F}$	Melt fraction	
H	Melt layer height	TBD
ρ_{ol}	Density of olivine	3200 kg/m^3
ρ_{wd}	Density of wadsleyite	3500 kg/m^3
ρ_m	Density of melt	3200–3400 kg/m^3
$\Delta\rho$	$(\rho_m - \rho_{ol})$	100–200 kg/m^3
χ^s_{ol}	Water content at olivine solidus	0.1 wt%
χ^s_{wd}	Water content at wadsleyite solidus	$>\chi^s_{ol}$?
χ^l_{ol}	Water content at olivine liquidus	~10 wt%
χ^l_{wd}	Water content at wadsleyite liquidus	$>\chi^l_{ol}$?
χ_{ol}	Water content of olivine above TZ	~0.1 wt%
χ_{wd}	Water content of wadsleyite in TZ	0.1–1.0 wt%
$\chi^\star_{wd}$	Water saturation of wadsleyite	~3.0 wt%
μ	Melt viscosity	~10 Pa s
η	Solid mantle viscosity	~10^{21} Pa s
g	Gravitational acceleration	9.81 m/s
w	Mantle vertical velocity at 410 km	
λ	Length of MPZ	
ℓ	Length of melt layer	
δ	Slab thickness	~100 km
v	Slab downwelling velocity	~10^{-9} m/s
α_h	Hydrous expansivity	~10^{-2}
D	Hydrogen diffusion	~10^{-7}–10^{-8} m^2/s
$2L$	Slab separation length	~10^3 km

solidus water contents. Above this point, melting occurs, where the melt is in equilibrium with wet, solid olivine.

[14] It should be noted that while we consider all melting and crystallization to be governed by local equilibrium for the purposes of this model, both the dehydration melting at the 410-km discontinuity and the entrainment of melt (in the VEZ and TEZ) are not equilibrium processes. Equilibrium is significantly disturbed in both cases by advection in an actively convecting mantle [*Richard et al.*, 2002]. Melt entrainment and production cannot be completely modeled by purely diffusive, equilibrium processes.

2.1. Melt Production Zone

[15] In the MPZ (denoted by $\mathcal{M}$ subscript), we first consider a small box of width dx, mass M, and height R, where the height of the melt layer is $H_\mathcal{M} < R$ (Figure 4). The change in mass with respect to time ($\frac{\partial M}{\partial t}$) of the box is equal to the net inward mass flux:

$$\frac{\partial M}{\partial t} = \Delta\rho\, dx \frac{\partial H_\mathcal{M}}{\partial t} = w\rho_{wd}\mathcal{F}dx + \bar{q}H_\mathcal{M}\rho_m|_x - \bar{q}H\rho_m|_{x+dx} \quad (2)$$

where w is the vertical velocity of the mantle at the base of the current, $\Delta\rho = \rho_m - \rho_{ol}$ is the density contrast between the melt and overlying solid olivine, and

$$\bar{q} = \frac{1}{H_\mathcal{M}} \int_0^{H_\mathcal{M}} v_x(z)\, dz \quad (3)$$

is the vertically averaged velocity in the melt layer. In the MPZ, interconnected networks and channels created by dehydration melting and subsequent compaction allow us to assume that melt spreading is controlled by the melt viscosity μ. Assuming that the channel obeys the lubrication approximations, that the pressure in the channel is hydrostatic, and that the boundaries of the current are effectively rigid leads to the following velocity profile in the current:

$$v_x(z) = \frac{\Delta\rho g}{2\mu} \frac{\partial H_\mathcal{M}}{\partial x} (z^2 - H_\mathcal{M} z) \quad (4)$$

where g is the gravitational acceleration. Combining equations (3) and (4) results in a vertically averaged flux of

$$\bar{q} = -\frac{\Delta\rho g H^2_\mathcal{M}}{12\mu} \frac{\partial H_\mathcal{M}}{\partial x} \quad (5)$$

[16] Using equation (5) in equation (2) yields the following evolution equation for the height of the melt layer in the MPZ:

$$\Delta\rho \frac{\partial H_\mathcal{M}}{\partial t} = w\rho_{wd}\mathcal{F} + \rho_m \frac{\Delta\rho g}{48\mu} \frac{\partial^2 H^4_\mathcal{M}}{\partial x^2} \quad (6)$$

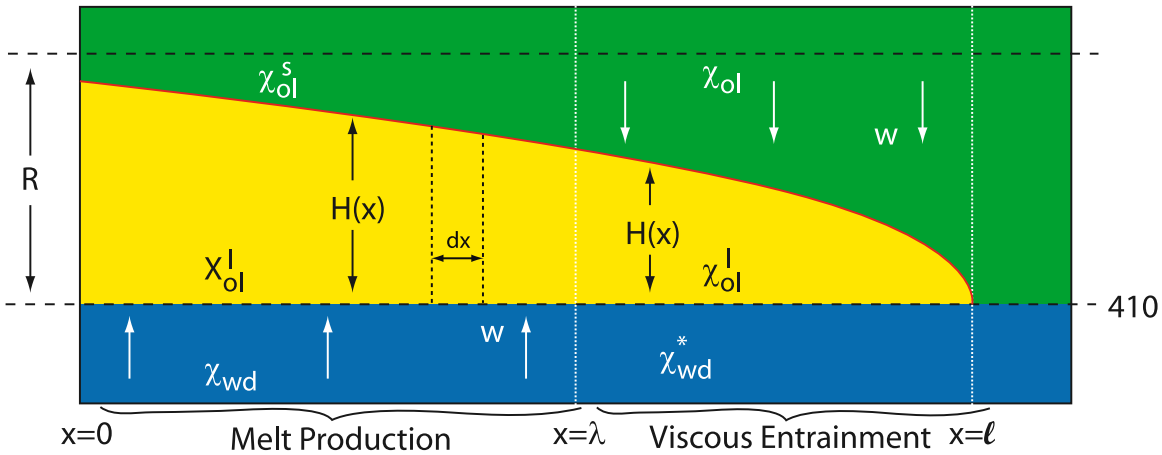

Figure 4. Gravity current model for melt layer spreading: Melt is produced in upwelling regions (left side) and spreads into downwelling regions (right side) where it is entrained. The mantle velocity field $w(x)$ determines the regions. Water contents χ are labeled in each region. A description of model parameters is presented in Table 1.

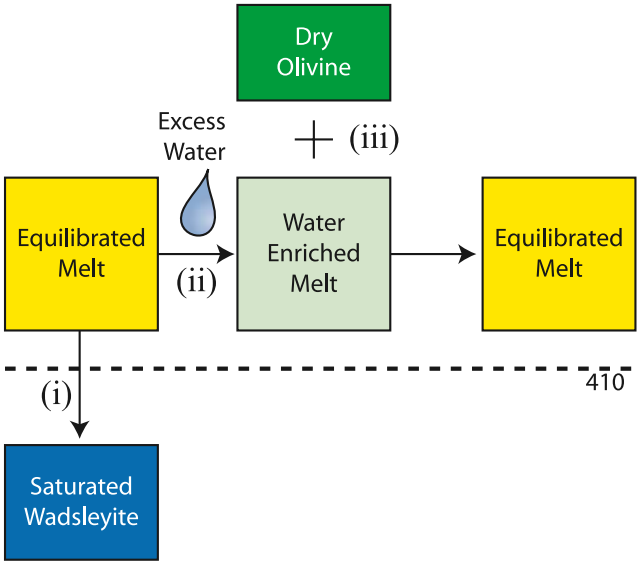

Figure 5. Mechanism for melt entrainment in the viscous entrainment zone: (i) Melt is advected below the 410-km discontinuity and crystallizes, resulting in saturated wadsleyite and residual water. (ii) The residual water enriches the melt layer, resulting in melt that is out of equilibrium with overlying olivine. (iii) Enriched melt reacts with the overlying olivine, returning the system to equilibrium.

2.2. Viscous Entrainment Zone

[17] As the melt layer spreads toward slabs, the mantle velocity field transitions from upward to downward and melt production ceases. In the absence of downward flow, melt layer spreading would be controlled by the viscosity of the overlying mantle [*Koch and Koch*, 1995]. However, in the presence of downward flow, we would expect melt layer spreading to be influenced by both chemical and mechanical interactions with background mantle. Consider, for example, a parcel of melt (with water content χ^l_{ol} forcibly advected below the 410-km discontinuity.

[18] Because the relevant phase equilibria for hydrated wadsleyite (liquidus, solidus, and solubility) have yet to be adequately determined, the parcel of melt at ambient mantle temperature could be either above or below the eutectic temperature T_e. Above T_e, we expect that the phase diagram for wadsleyite resembles that of olivine (Figure 3). In this case, assuming higher solidus and liquidus water contents (χ^s_{wd} and χ^l_{wd}, respectively, in weight percent), the melt parcel (with water content χ^l_{ol} such that $\chi^s_{wd} < \chi^l_{ol} < \chi^l_{wd}$) repartitions into a solid wadsleyite and a wet "wadsleyite" melt.

[19] Below T_e, we expect that all of the silicates in the melt crystallize into water-saturated wadsleyite ($\chi^\star_{wd}$), in equilibrium with the excess free water. Regardless of whether the melt falls above or below T_e, the resulting solid and fluid are not in equilibrium with the original melt. The mass of water that can be removed by the entrained solid from the parcel of melt via these two different crystallization scenarios is well below the melt's total water content; this results in silicates being removed at a greater rate than is water (Figure 5i). More realistically, these crystallization processes would occur at the phase change interface, and the resulting fluid or melt, having higher concentration of water and hence more buoyant, would be immediately remixed back into the melt layer. Both cases therefore enrich the melt layer in water (Figure 5ii). We will assume for subsequent derivations that wadsleyite is subeutectic below the 410 km although the equations can be trivially modified to account for the supereutectic case.

[20] Because the water content of the enriched melt now exceeds the liquidus value, it is out of equilibrium with the dry olivine solid above it. The melt therefore loses water to the overlying olivine, which in turn melts, diluting the melt and driving the system toward equilibrium. This melting will occur just at the interface between the melt and the overlying solid. The assumption of a dense melt precludes the existence of reactive fingering instabilities [*Aharonov et al.*, 1997; *Aharonov et al.*, 1995; *Kelemen et al.*, 1995] on this interface, and instead the melt layer should remain segregated. This model describes both the processes of entraining water in downwelling mantle and how the melt layer spreads through the reactive melting process.

[21] For the VEZ (denoted by $\mathcal{V}$ subscript), the derivation of an evolution equation follows the same logic as for the MPZ (see equations (2), (3), (4), (5), and (6)):

$$\Delta\rho\frac{\partial H_\mathcal{V}}{\partial t} = s(x) + \rho_m\frac{\Delta\rho g}{48\mu}\frac{\partial^2 H^4_\mathcal{V}}{\partial x^2} \tag{7}$$

[22] In steady state, the flow of field in the melt channel is controlled by the melt viscosity μ rather than the viscosity of overlying olivine η. The source $s(x)$ is the net flow into the melt layer, accounting for wadsleyite entrained through the bottom and the resultant melting of the overlying olivine to return the system to equilibrium (see Appendix A for derivation):

$$s(x) = w\rho_m\left(\frac{1-\chi^l_{ol}}{1-\chi^\star_{wd}}\right)\left(\frac{\chi^\star_{wd}-\chi_{ol}}{\chi^l_{ol}-\chi_{ol}}\right) \tag{8}$$

Note that, in this case, w is negative due to the downwelling, and χ_{ol} is the water content of the overlying olivine ($\chi_{ol} \le \chi^s_{ol}$).

2.3. Steady State Solutions

[23] Using evolution equations (6) and (7) and assuming that the solution reaches steady state, we can solve for $H = H(x)$ for the entire melt layer. Here and in subsequent derivations, the MPZ extends from 0 to λ (where $w(\lambda) = 0$), and the VEZ extends from λ to ℓ. We apply the following boundary conditions: At the center of the MPZ, assuming a symmetric velocity field, there should be no horizontal fluid flux and therefore no gradient in melt layer height:

$$\frac{\partial H_\mathcal{M}}{\partial x} = 0, \qquad \text{at } x = 0 \tag{9}$$

[24] At the nose of the current, its height should vanish:

$$H_\mathcal{V} = 0, \qquad \text{at } x = \ell \tag{10}$$

[25] At the boundary between the MPZ and the VEZ, the height of the gravity current and the horizontal fluid flux should be continuous:

$$\begin{cases} H_\mathcal{M} = H_\mathcal{V} \\ \dfrac{\partial H_\mathcal{M}}{\partial x} = \dfrac{H_\mathcal{V}}{\partial x}, \end{cases} \qquad \text{at } x = \lambda. \tag{11}$$

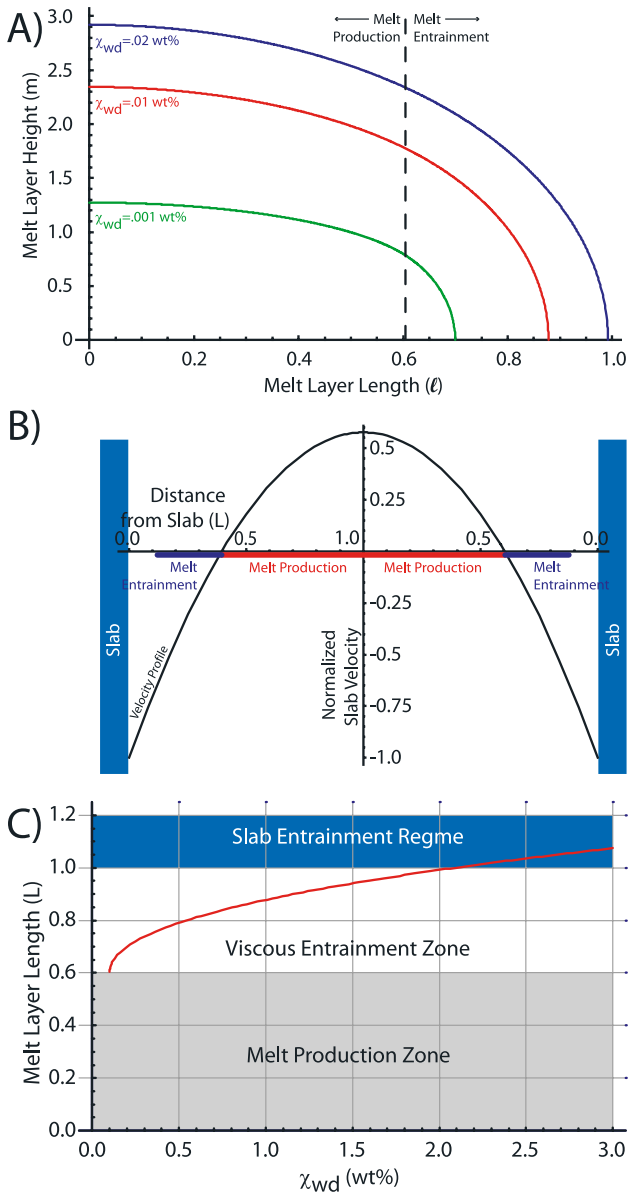

Figure 6. Melt layer predictions: (a) melt layer structure for different water contents. The horizontal axis is in units of L, where 1 is the slab interface. The height of the melt layer is given in meters and does not exceed 3 m for plausible transition zone water contents given a Poiseuille flow background velocity profile (second frame). (b) For a given water content and velocity profile, the calculated MPZ (red) and VEZ (blue) are highlighted. (c) For a given transition zone water content, using the same velocity profile as in Figure 6b, the total melt layer length is plotted.

[26] In steady state, the integrated mass source term in the MPZ [from equation (6)] should balance the integrated source term in the VEZ [equation (8)]:

$$\int_0^{\lambda} \rho_{wd} w \left(\frac{\chi_{wd}-\chi_{ol}^s}{\chi_{ol}^l-\chi_{ol}^s}\right) dx = -\int_{\lambda}^{\ell} \rho_m w \left(\frac{1-\chi_{ol}^l}{1-\chi_{wd}^s}\right)\left(\frac{\chi_{wd}^s-\chi_{ol}}{\chi_{ol}^l-\chi_{ol}}\right) dx \tag{12}$$

[27] In steady state, evolution equations (6) and (7) give the following equations for melt layer height:

$$H_{\mathcal{M}}^4 = \frac{48\mu}{\Delta\rho g}\frac{\rho_{wd}}{\rho_m}\left(\frac{\chi_{wd}-\chi_{ol}^s}{\chi_{ol}^l-\chi_{ol}^s}\right)\iint w(x)\,dx^2 + \aleph_0 x + \aleph_1 \tag{13}$$

$$H_{\mathcal{V}}^4 = \frac{48\mu}{\Delta\rho g}\left(\frac{1-\chi_{ol}^l}{1-\chi_{wd}^s}\right)\left(\frac{\chi_{wd}^s-\chi_{ol}}{\chi_{ol}^l-\chi_{ol}}\right)\iint w(x)\,dx^2 + \aleph_2 x + \aleph_3 \tag{14}$$

[28] The constants $\aleph_0$, $\aleph_1$, $\aleph_2$, and $\aleph_3$ can be solved by applying boundary conditions (9), (10), (11), (12).

[29] Assuming a geometry of flow driven by two descending slabs, we derive a flow field w that we use to drive the melt layer system, and we then solve for steady state solutions. Solutions for height of the melt layer, given simple Poiseuille flow between slabs, are presented in Appendix B. In Figure 6a, we show solutions for melt layer structure for different upwelling water contents (χ_{wd}). We find that the maximum predicted melt layer height is weakly dependent on water content and does not exceed 3 m for plausible water contents. Figure 6b shows the calculated melt layer regimes for the displayed velocity profile.

[30] In general, because the total length of the melt layer is constrained by the fluxes of water inward through melting and outward through entrainment, a TZ that is originally undersaturated in water in the MPZ would result in a small entrainment region. We can derive a simple scaling law for the ratio of the length of the VEZ to that of the MPZ, assuming a simple step function velocity profile,

$$w(x) = \begin{cases} +w & \text{for } x \le \lambda \\ -w & \text{for } x > \lambda \end{cases} \tag{15}$$

in equation (12) to obtain the ratio of the length of the VEZ to that of the MPZ:

$$\frac{\ell-\lambda}{\lambda} = \frac{\rho_{wd}}{\rho_m}\left(\frac{\chi_{wd}-\chi_{ol}^s}{\chi_{ol}^l-\chi_{ol}^s}\right)\left(\frac{1-\chi_{wd}^\star}{1-\chi_{ol}^l}\right)\left(\frac{\chi_{ol}^l-\chi_{ol}}{\chi_{wd}^\star-\chi_{ol}}\right) \tag{16}$$

[31] With water contents of upwelling TZ material χ_{wd} between 0.2 and 1.0 wt%, and the water content of downwelling olivine $\chi_{ol} = \chi_{ol}^s$ (residual from initial dehydration melting), the length of the entrainment region ℓ-λ ranges from 3 to 33% of that of the upwelling region λ. The melt layer is therefore not expected to spread far from the MPZ.

[32] When we consider the case of a parabolic velocity profile, entrainment becomes increasingly efficient as the melt layer spreads toward the slab. Because we assume homogeneous water content in the transition zone in the upwelling region (which is fixed in space), the flux of water into the melt via melting is simply proportional to the upwelling water content, whereas the flux of mass out of the melt channel is proportional to the integral of downwelling velocity. Because the downwelling velocity increases as the melt spreads toward the slab, the entrainment flux of water also increases, leading to more efficient entrainment (Figure 6c). Note that for water contents exceeding ~2 wt% (close to saturation), the melt layer will always reach the slab, requiring a more careful consideration of the thermal regime.

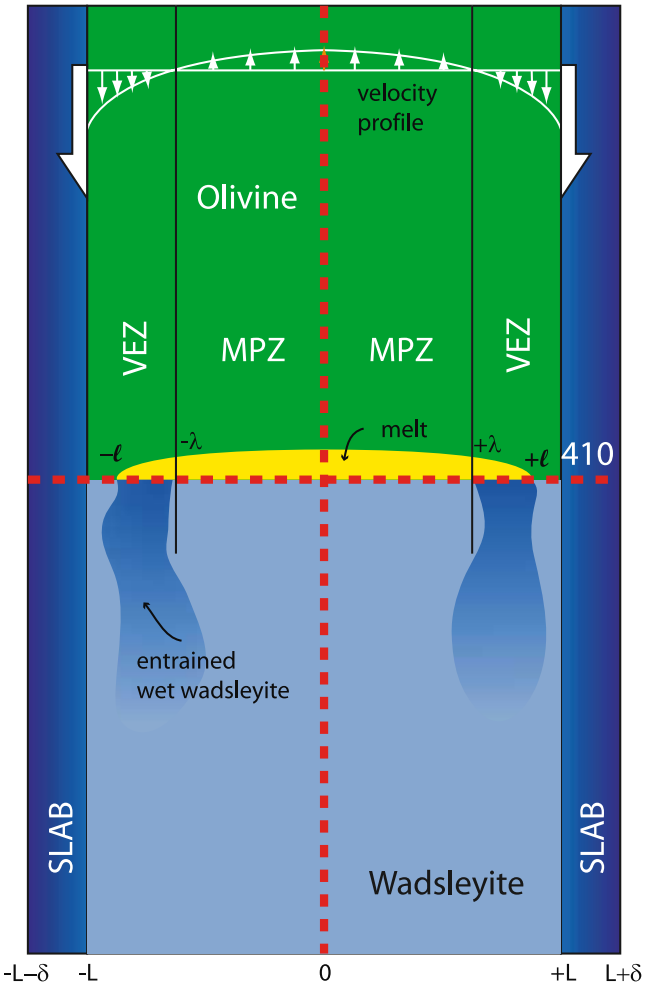

Figure 7. Model of melt entrainment perturbing background flow field: Buoyancy anomalies entrained by slab-driven Poiseuille flow disturb the background flow, which in turn affects melt production and spreading.

[33] An important consequence of the proposed entrainment mechanism is that, because the wadsleyite is entrained at saturation (and due to the fact that wadsleyite can hold a significant amount of water), it is more buoyant than the surrounding, undersaturated transition zone materials. This buoyancy difference is large enough to affect the mantle flow field and therefore has an important influence on the melt layer. One can hypothesize that the result of this effect will be to reduce the efficiency of entrainment by slowing downward flow across the 410-km discontinuity in the VEZ. This effect will be explored in the following section.

3. Effect of Entrainment on Mantle Flow

[34] Water saturated wadsleyite may be as much as 50–100 kg/m^3 less dense than dry wadsleyite [*Angel et al.*, 2001], and therefore the proposed entrainment mechanism has the potential to disturb the slab-driven mantle flow field. To examine this problem in more detail, we consider two-dimensional flow between two parallel slabs of infinite length and thickness δ moving downward at a constant rate, $v < 0$. We thus determine how the flow between the slabs is perturbed by the addition of small, compositional density anomalies. The flow model will be coupled to the melt layer model via the background flow at a reference depth (which will drive melt production and entrainment), and the melting and entrainment will be used as sources and sinks of water for chemical circulation (Figure 7).

[35] For this problem, we consider the bulk fluid to obey the Boussinesq approximation (chemical density anomalies are negligible unless coupled to g), isoviscous, isothermal, and with infinite Prandtl number. The bounding slabs are rigid and impenetrable to water. The equations of mass, momentum, and water conservation (nondimensionalized by length scale L, timescale $\frac{L^2}{D}$, and concentration scale χ_0) lead to dimensionless governing equations for water content χ, and velocity stream function ψ (such that velocity $v = \nabla \times \psi\hat{\mathbf{y}}$):

$$\frac{\partial \chi}{\partial t} - \hat{\mathbf{y}} \cdot (\nabla\psi \times \nabla\chi) = \nabla^2\chi \tag{17}$$

$$\nabla^4\psi + B\frac{\partial \chi}{\partial x} = 0 \tag{18}$$

$$B = \frac{\rho_0 g \alpha_h \chi_0 L^3}{D\eta} \tag{19}$$

is the buoyancy number, which governs the vigor of buoyantly driven flow. Moreover, ρ_0 is a reference density, g is gravity, χ_0 is a reference water concentration, $2L$ is the distance between slabs, D is the hydrogen diffusion coefficient, and η is the solid mantle viscosity. The parameter α_h describes expansion due to hydration and can be inferred by comparing experimental data to the density model $\rho = \rho_0 (1 - \alpha_h(\chi - \chi_0))$. Given Earth-like parameters, $\alpha_h \sim 10^{-2}$ [*Angel et al.*, 2001], and $B \sim 10^5$. One other governing parameter is the nondimensional downwelling slab velocity V:

$$V = \frac{vL}{D} \tag{20}$$

[36] The boundary conditions on flow between the slabs are that, at the slab interfaces, $x = \pm 1$, and $v = (0, v)$; in addition, as $z \to \pm\infty$, $\psi \to \psi_P(x)$, the Poiseuille flow solution. We only solve for water concentration below the 410-km discontinuity, assuming that the melting homogenizes the mantle above the transition zone. Above 410 km, $\chi = \chi_0 \sim 0.1$ wt%. Sources of water are implemented as boundary conditions at the 410-km discontinuity. In the downwelling regions where melt is entrained ($|x| < \ell$), $\chi = \chi^s_{wd} \sim 3$ wt%. In downwelling regions where melt is produced ($|x| < \lambda$) or is not entrained ($|x| > \ell$), $\chi = \chi_0$. Additionally, we assume that at the slab interfaces ($x = \pm 1$), $\chi = \chi_0$, and that there is no lateral water flux. As $z \to -\infty$, $\chi \to \chi_0$.

$$\begin{aligned}
\text{At } z = \pm\infty &: \begin{cases} \psi = \psi_P \\ \chi = \chi_0 \end{cases}, \\
\text{At } z = 0\,(410\text{ km}) &: \begin{cases} \chi = \chi_0; & \text{if } |x| > l \\ \chi = \chi^\star_{wd}; & \text{if } |x| < l \\ \chi = \chi_0; & \text{if } |x| < \lambda \end{cases}, \\
\text{At } x = \pm 1 &: \begin{cases} \dfrac{\partial \psi}{\partial x} = -V; \ \dfrac{\partial \psi}{\partial z} = 0 \\ \chi = \chi_0; \quad \dfrac{\partial \chi}{\partial x} = 0 \end{cases}
\end{aligned} \tag{21}$$

[37] In the absence of density anomalies, the Poiseuille flow solution ψ_P automatically satisfies the boundary conditions, so we can rewrite the stream function following the work of *Katopodes et al.* [2000] as:

$$\psi = \psi_P + \psi' \tag{22}$$

where $\psi_P = \frac{-V}{2}(x^3 - x)$, which satisfies the homogeneous biharmonic equation. The perturbation stream function ψ' is subject to the following boundary conditions:

$$\begin{aligned} \psi' &= 0 \quad \text{at } z = \pm\infty \\ \frac{\partial \psi'}{\partial x} &= \frac{\partial \psi'}{\partial z} = 0 \quad \text{at } x = \pm 1 \end{aligned} \tag{23}$$

[38] This yields the modified governing equations:

$$\frac{\partial \chi}{\partial t} - \hat{\mathbf{y}} \cdot (\nabla(\psi_P + \psi') \times \nabla\chi) = \nabla^2\chi \tag{24}$$

$$\nabla^4\psi' + B\frac{\partial \chi}{\partial x} = 0 \tag{25}$$

[39] Following the method described by *Zhong* [1996], we derive solutions to the biharmonic equation forced by a density field. We first consider a Green's function solution to the equation:

$$\nabla^4 G(x,z;x',z') = \delta(x-x')\delta(z-z') \tag{26}$$

It can be shown that

$$G(x,z;x',z') = \sum_n \frac{\sin(k_n x')\sin(k_n x)}{4k_n^3}(1 + k_n|z-z'|)e^{-k_n|z-z'|} \tag{27}$$

where $k_n = n\pi$, satisfies the momentum equation and can therefore be convolved with the density gradient function to solve for the flow field, i.e.,

$$\psi'(x,z) = \iint_{\mathcal{D}} -B\frac{\partial \chi(x',z')}{\partial x} G(x,z;x',z')\, dx'dz' \tag{28}$$

where $\mathcal{D}$ is the domain of integration.

[40] The dynamic, slab-driven flow model is coupled to the steady state melt layer model via boundary conditions at the 410-km discontinuity. In order to consistently apply the steady state model to this dynamic problem, the change in melt layer shape (and therefore length $\Delta\ell$) with each time step Δt must be small such that we can assume that the adjustment in background flow to changes in chemical buoyancy is instantaneous. This allows the definition of a melt layer "spreading rate" $\mathcal{U} = \frac{\Delta\ell}{\Delta t}$. We assume that, if $\mathcal{U} < 0.1V$, the rate of melt spreading is much less than typical bulk mantle velocities, and we can define the melt spreading as "quasi-steady".

[41] The quasi-steady cases are then assumed to be valid extensions of the steady state model. We then look for solutions using a range of buoyancy and velocity parameters ($10^4 < B < 10^7$, $10^2 < V < 10^6$). A diagram of the parameter space is given in Figure 8.

[42] Analysis of the flow field (Figure 9) indicates that water entrained from the melt layer significantly disturbs the slab-driven flow pattern. In particular, we find that entrained, hydrated (and therefore buoyant) wadsleyite tends to spread horizontally away from the VEZ as indicated by the velocity vectors in Figure 9. This is because the buoyancy anomaly leads to the development of a pressure high in the TZ below the VEZ. Horizontal spreading toward the slab is easily overwhelmed by the large downward slab velocity, whereas the limited vertical flow near the boundary between the MPZ and the VEZ provides little resistance to horizontal spreading.

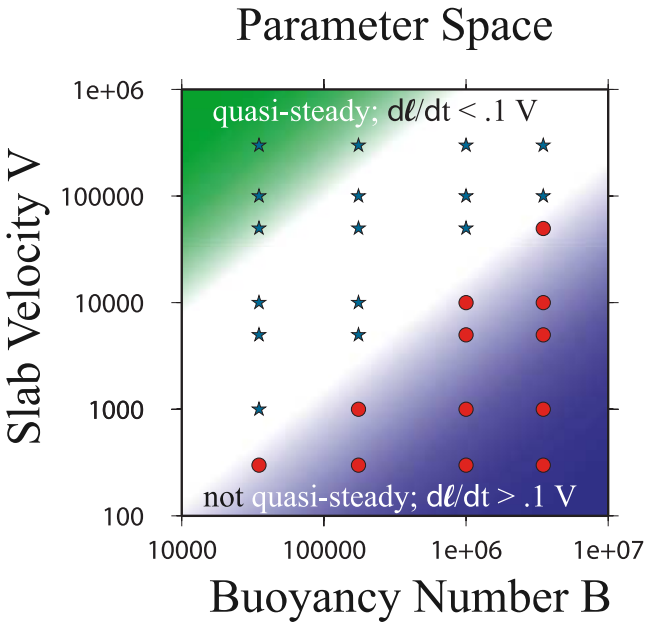

Figure 8. Governing parameters for the coupled entrainment-flow model are buoyancy number B and nondimensional slab velocity V. Stars represent simulations where melt layer spreading can be considered "quasi-steady," i.e., melt spreading is much slower ($\Delta\ell/\Delta t < 0.1\ V$) than the downwelling velocity. Circles represent simulations where melt spreading is not "quasi-steady" ($\Delta\ell/\Delta t > 0.1\ V$). Shaded regions of the parameter space represent the regimes where entrainment dominates (green), where buoyant spreading dominates (blue), and where there is competition between the two (white). All cases where the melt spreads as far as geometrically possible correspond to "nonquasi-steady" cases.

[43] One effect of the horizontal spreading of hydrated material in the transition zone is to inhibit entrainment near the boundary between the VEZ and the MPZ. In fact, the buoyant hydrated wadsleyite can shut off entrainment due to downwelling completely, causing the melt production region to expand. The central, upwelling region of the vertical velocity profile at the 410-km boundary tends to broaden and decrease in vigor. At the same time, the width of the VEZ decreases in size due to increased efficiency of entrainment [similar to the effect described by equation (16)]. The buoyant anomalies near the slabs have the dynamic effect of weakening the downward flow near slabs, which is necessarily accompanied by a corresponding decrease in upward flow. The net effect is to weaken the maximum upwelling velocity, in some cases, by up to a factor of 25%.

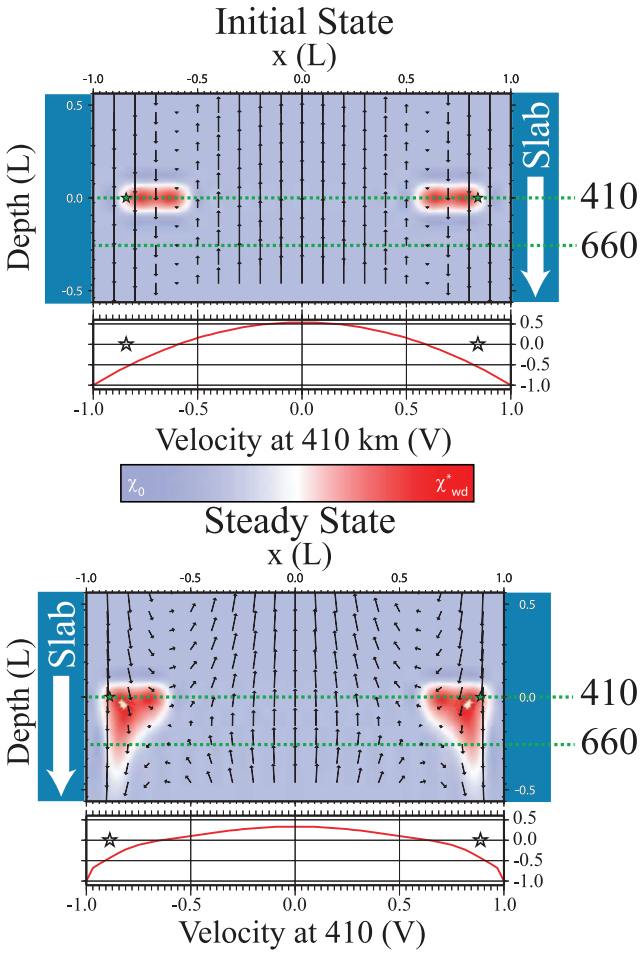

Figure 9. Flow field for coupled melt entrainment model: Plotted is the water concentration field for the initial and final states. Regions of high water content (red) are located in the transition zone beneath the VEZ. In steady state, the melt layer has spread closer to the slab from its initial state, and the VEZ is smaller. Black arrows represent the mantle flow field. The vertical velocity profile at the 410-km discontinuity is plotted below each frame, and it broadens in shape and shrinks in amplitude in steady state. The black stars represent the maximum lateral extent of the current ℓ.

[44] In addition to these dynamic effects on the mantle flow field, the horizontal spreading of hydrated material in the TZ also acts to rehydrate the upwelling regions. This model would predict that a portion of upwelling mantle near the boundary between the VEZ and the MPZ may have water contents that are very close to saturation.

[45] In steady state, this chemical cycling helps to retain water in the TZ. However, our model neglects dehydration processes that may occur as hydrated material passes through the 660-km discontinuity and into the lower mantle [*Richard et al.*, 2006, 2007], where the dominant phases can accommodate less water [*Bolfan-Casanova et al.*, 2003]. In our simulations, there is a relatively large flux of hydrated material into the lower mantle, and we may therefore underestimate both the retention and remixing of water in the transition zone and the magnitude of horizontal spreading.

[46] For every case that we have examined, we find that, after a brief adjustment, the melt layer achieves a steady state structure that accounts for changes to flow due to buoyant anomalies in the transition zone. We can define a dimensionless quantity $\mathcal{R}$, which represents a resistance to entrainment, as

$$\mathcal{R} = \frac{B}{V} = \frac{\rho_0 g \alpha_h \chi_0 L^2}{\nu \eta} \tag{29}$$

[47] We find that, for values of $\mathcal{R} < 10^2$, the model is indeed in the quasi-steady regime (Figure 8, blue stars), and we can be confident in the interpretation of our results. For values of $\mathcal{R} > 10^2$, the adjustment period is characterized by rapid changes in melt layer length, and the quasi-steady assumption is violated (Figure 8, red circles). Yet these cases also attain a steady structure.

[48] We also examine how the steady state length of the current is controlled by the governing parameters in order to determine how close to the slab (and therefore the TEZ) the melt approaches. Our results clearly show (Figure 10) that, for a given buoyancy number B, the current moves through three distinct regimes as the slab velocity V is increased. First, for low V, buoyant spreading dominates and the melt spreads until it is forcibly entrained by the slab (due to the no-slip boundary condition). This corresponds to values of $\mathcal{R} > 10^2$ (Figure 8, shaded blue) and also coincides with the nonquasi-steady cases. As V increases, competition between buoyant spreading and downward entrainment of water ensues (Figure 8, $1 < \mathcal{R} < 10^2$, shaded white). As velocity increases further, it completely dominates the entrainment process, and the extent of the melt layer reverts to the Poiseuille flow solution discussed in the previous section

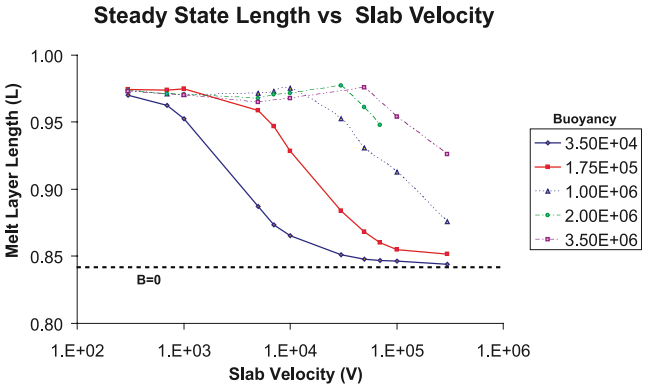

Figure 10. Melt layer length versus slab velocity V for different buoyancy numbers B, with upwelling wadsleyite water content $\chi_{wd} = 1$ wt%. Three regimes can be identified: the low V, large l regime represents the case when buoyant spreading dominates over entrainment, with the melt layer spreading until it is forcibly entrained via the no-slip slab boundary condition. The large V, small l regime represents the case when downwelling velocity is so strong that buoyancy has little effect, and the melt layer reverts to the Poiseuille flow solution. The third regime represents the case where buoyant spreading competes with entrainment. Decreasing χ_{wd} results in a downward translation and broadening of these curves, consistent with the results shown in Figure 6c.

(Figure 8, $\mathcal{R} < 1$, shaded green). Our results also indicate that, with increasing water content in the upwelling wadsleyite, the melt layer extends closer to the slab interface in a manner that is consistent with the predictions when perturbations to the flow field are neglected (as in Figure 6c).

4. Discussion

[49] The two-dimensional steady state melt layer model predicts a very thin melt layer on the order of meters; this prediction is relatively insensitive to changes in model parameters such as density and water content. This result is not unexpected because our model does not have a source that depends explicitly on height, which in steady state might act to thicken the melt layer. These results, however, may be an effect of the simplifying assumptions in our model. For example, if we were to model a partial melt instead of the decompacted melt lens that we study here, the height of the melt region could increase. Also, if the melt layer reaches the cold slab regime, diffusion of water may play a significant role in permitting a thicker molten region [*Bercovici and Karato*, 2003]. Regardless, if the VEZ does play a significant role in melt recycling, we would expect thinner rather than thicker melt layers.

[50] Furthermore, we assume in our model that there is no topography on the 410-km discontinuity. In fact, the depth of the discontinuity varies probably by tens of kilometers, primarily because of variations in temperature and water content [*Wood*, 1995]. If topography at the discontinuity were included in our simple model, the melt would accumulate in troughs and possibly inundate crests, depending on the lateral extent reached by the melt layer before entrainment balances melt production. The eventual thickness of the melt would be dominated by the topographic signal ($\mathcal{O}(10)$ km), which is much larger than the changes in melt layer thickness necessary to drive flow in steady state. This type of melt accumulation would be seismically observable.

[51] Additionally, we consider only the steady state solutions for melt layer shape. When melt is being produced, and spreads away from the MPZ, the spreading rate will be dominated by the viscous stresses necessary to displace the overlying mantle. This would require a thicker melt layer to provide an adequate pressure head. Once the melt spreads into the entrainment region, the surface melting reaction may help to mitigate this effect, but the dynamic interaction between the viscous and chemical forcings needs to be examined in greater detail before drawing more robust conclusions.

[52] Another effect that will act to influence the thickness and shape of the melt layer concerns the latent heat effect on water solubility. This implies that cooling due to melting will reduce the water transferred to the melt layer (both in the MPZ and the surface melting of the VEZ) and that warming due to crystallization in the VEZ will further reduce the efficiency of entrainment. Additionally, gradients in temperature and therefore water solubility will force diffusion in the melt layer. To model these effects will require full thermal modeling in the regions surrounding the 410-km discontinuity.

[53] Though our mechanism for melt entrainment only necessitates a thin melt layer, making seismic testing problematic, it has several other consequences which could be tested by seismic observations. In particular, our model predicts strong heterogeneity in transition zone water content, especially between regions of melt production (undersaturated) and melt entrainment (near-saturated). Tests would include correlations of seismic velocity, seismic attenuation, and electrical conductivity with inferred models for mantle flow. *Lawrence and Wysession* [2006] describe how water-rich regions near slabs can be inferred from seismic measurements: We would expect slightly lower-than-average seismic velocities yet higher-than-average attenuation to correlate strongly with regions of downward flow.

[54] In fact, *Obayashi et al.* [2006] have recently observed a low-velocity region around the 410-km discontinuity oceanward from the subducted Pacific plate. Though they postulate a purely thermal cause for the anomaly, it is possible that it may represent the entrainment process described here. Both the broad extent and the location near the downwelling slab correspond plausibly with our model, especially given elevated transition zone water contents in the Pacific [*Huang et al.*, 2005]. If the results shown in Figure 9 were to correspond to the Pacific, with $L \sim 5000$ km, we would predict a water-rich anomaly in the transition zone of roughly 500–1000 km. While *Obayashi et al.* [2006] note that enrichment in water is known to elevate the phase transition (opposing their observations of a depressed 410-km discontinuity), excess latent heat released by the crystallization of wadsleyite in the VEZ (potentially resulting in a temperature increase of several hundred degrees) could counter the effect of hydration and might even result in a depression of the discontinuity.

[55] Consequences of this model with respect to trace element circulation in the mantle include the fact that, since incompatible elements tend to follow water, many heat-producing elements may be trapped in the transition zone, resulting in an enriched layer in the middle of the mantle. Previous results have indicated that, as long as the sequestering is incomplete, this will not disturb the slab-driven convective planform observed in Earth [*Leahy and Bercovici*, 2004]. However, we might also expect to see heterogeneous lateral distribution of incompatible elements in the TZ. Local enrichment in heat-producing elements may serve to intensify the buoyancy anomalies caused by entrained water and could therefore further disturb the mantle flow field (though faster thermal diffusion would help mitigate this effect). Hypothetically, an excessively buoyant region of past entrainment that is enriched in water and trace elements could develop into a source for a mantle plume.

[56] A significant prediction of our model is that ambient upwelling flow in the mantle can be both broadened and slowed down by melting above the transition zone. This implies that the main downward flux of both bulk and trace elements is constrained to material in the immediate vicinity of a cold slab's thermal halo. Additionally, slower upwelling velocities will inhibit the remixing of subducted material into the mantle and may significantly increase the residence time of chemical anomalies in the mantle.

[57] As the velocity profile flattens and broadens, the residence time and age distribution narrows: A greater mass of material shares the same residence time. This effect contributes to the homogeneity of the MORB source as

evident in MORB isotope arrays [*Van Keken et al.*, 2002; *Hofmann*, 1997].

[58] Our model also indicates that a significant mass of water may be trapped in vortices centered, where the bulk velocity field transitions from upwelling to downwelling that would never have an expression on the surface, but yet might form a substantial global reservoir.

[59] Extensions of our flow model to more complicated rheologies would not influence our results significantly. In fact, a temperature-dependent viscosity would strengthen our assumption of an isothermal temperature field in the mantle surrounding slabs because material falling within the thermal halo around slabs will be considerably more viscous than mantle at ambient temperatures and thus would be viewed by the surrounding mantle as rigid (what we call slab in our model).

[60] In conclusion, we find that the entrainment of wet wadsleyite is an extremely effective mechanism to return water from a hydrous melt layer above the 410 km to the transition zone. Melt spreading in downwelling regions of the mantle flow field relies on a reaction of the melt with overlying solid olivine. Entrainment creates wet, buoyant anomalies in the TZ, which spread horizontally, resulting in a broader, less vigorous mantle flow field. We also propose that evidence of melt entrainment could be visible in the seismic data near slabs as areas of large seismic attenuation with only a minor decrease in shear wave speed. Further directions for modeling include solving the full time-dependent gravity current equations for the evolution of melt layer structure by including the competition between viscous spreading and the melting reaction in the entrainment region. Predictions of melt layer structure and entrainment that permit full temperature dependence for water circulation may also be necessary to create meaningful predictions of geochemical structure in the mantle.

Appendix A: Melt Sources and Sinks

[61] Here we present the derivations for the sources and sinks of melt for the two-dimensional melt layer model. In the melt production zone (MPZ), the flux of melt into the layer is $w\rho_{wd}\mathcal{F}dx$, where $\mathcal{F}$ is given by equation (1). This can be broken down into a water flux $w\rho_{wd}\mathcal{F}\chi^l_{ol}dx$ and a silicate flux $w\rho_{wd}\mathcal{F}(1-\chi^l_{ol})$dx.

[62] The net flux of material out of the viscous entrainment zone (VEZ) is more complicated. First, consider a flux of melt downward out of the layer $w\rho_m dx$, which can again be broken down into a water flux $w\rho_m\chi^l_{ol}dx$ and a silicate flux $w\rho_m(1-\chi^l_{ol})dx$. All of the silicate flux is assumed to crystallize as saturated wadsleyite. The total mass sink due to entrainment is then $\gamma\rho_{wd}dx$, where the silicate flux is:

$$\gamma\rho_{wd}(1-\chi^\star_{wd})\,dx = w\rho_m(1-\chi^l_{ol})\,dx$$
$$\Rightarrow \gamma = w\frac{\rho_m}{\rho_{wd}}\left(\frac{1-\chi^l_{ol}}{1-\chi^\star_{wd}}\right) \tag{A1}$$

[63] The amount of water removed via crystallization is $\gamma\rho_{wd}\chi^\star_{wd}$, or

$$w\rho_m\chi^s_{wd}\left(\frac{1-\chi^l_{ol}}{1-\chi^\star_{wd}}\right)dx \tag{A2}$$

Thus, by subtracting the mass of water removed via crystallization [equation (A2)] from the amount of water advected below the phase boundary ($w\rho_m\chi^l_{ol}dx$), we arrive at the mass of water rejected via the crystallization process that remains to enrich the melt layer, which is:

$$w\rho_m\left(\frac{\chi^l_{ol}-\chi^\star_{wd}}{1-\chi^\star_{wd}}\right)dx \tag{A3}$$

Equation (A3) represents the amount of water that will react with the overlying olivine to return the system to equilibrium. Assuming that melting occurs during this reaction, we can postulate that $\zeta\rho_{\rm ol}dx$ olivine reacts with the excess water to produce $\xi\rho_{\rm m}dx$ melt. This yields the following two equations for silicate and water conservation:

silicates:

$$\zeta\rho_{ol}(1-\chi_{ol})\,dx = \xi\rho_m(1-\chi^l_{ol})dx \tag{A4}$$

water:

$$\zeta\rho_{ol}\chi_{ol}dx + w\rho_m\left(\frac{\chi^l_{ol}-\chi^\star_{wd}}{1-\chi^\star_{wd}}\right)dx = \xi\rho_m\chi^l_{ol}dx \tag{A5}$$

where χ_{ol} is the mass fraction of water contained in the overlying solid olivine. These two equations can be solved for ζ and ξ, giving

$$\zeta = w\frac{\rho_m}{\rho_{ol}}\left(\frac{\chi^l_{ol}-\chi^\star_{wd}}{\chi^l_{ol}-\chi_{ol}}\right)\left(\frac{1-\chi^l_{ol}}{1-\chi^\star_{wd}}\right) \tag{A6}$$

$$\xi = w\left(\frac{\chi^l_{ol}-\chi^\star_{wd}}{\chi^1_{ol}-\chi_{ol}}\right)\left(\frac{1-\chi_{ol}}{1-\chi^\star_{wd}}\right) \tag{A7}$$

[64] The net mass flow out of the melt layer due to entrainment is therefore:

$$\gamma\rho_{wd}dx - \zeta\rho_{ol}dx = w\rho_m\left(\frac{1-\chi^l_{ol}}{1-\chi^\star_{wd}}\right)\left(\frac{\chi^\star_{wd}-\chi_{ol}}{\chi^l_{ol}-\chi_{ol}}\right)dx \tag{A8}$$

Appendix B: Melt Layer Structure for Poiseuille Flow

[65] Given evolution equations (13) and (14) for steady state melt layer structure and the velocity field w, we can calculate the height and length of the melt layer atop the 410-km boundary. For simplicity, we will consider upward Poiseuille flow driven between two parallel slabs descending into the mantle. In this geometry, the velocity profile satisfies the momentum equation $0 = \frac{\partial p}{\partial z} + \eta\frac{\partial^2 w}{\partial z^2}$. We can solve for the pressure gradient $\frac{\partial p}{\partial z}$ by specifying that the net mass flux through a horizontal plane is zero:

$$\rho_0\int_{-1}^{1} w dx - \rho_0 v\delta = 0 \tag{B1}$$

yielding a vertical velocity at 410 km of:

$$w(x) = \frac{3v}{2}\left(1+\frac{\delta}{2}\right)(x^2-1)+v \tag{B2}$$

In equations (B1) and (B2), v is the slab's vertical velocity, ρ_0 is a reference density, and δ is the slab thickness. The boundaries between melt production and entrainment are the roots of the velocity profile [equation (B2)] for $w = 0$, and therefore the length of the MPZ λ is:

$$\lambda = \left| \sqrt{1 - \frac{1}{\frac{3\delta}{4} + \frac{3}{2}}} \right| \tag{B3}$$

[66] The total length of the current l can be determined via the mass flux boundary condition by integrating the source terms due to melting and entrainment along the length of the current as in equation (12):

$$0 = \int_0^{\lambda} w(x)\rho_{wd}\left(\frac{\chi_{wd} - \chi_{ol}^s}{\chi_{ol}^l - \chi_{ol}^s}\right)dx + \int_{\lambda}^{\ell} w(x)\rho_m\left(\frac{1-\chi_{ol}^l}{1-\chi_{wd}^s}\right)\left(\frac{\chi_{wd}^s - \chi_{ol}}{\chi_{ol}^l - \chi_{ol}}\right)dx \tag{B4}$$

and thus is the root of the following equation:

$$0 = \ell^3 + 3\left(\frac{v}{\Gamma} - 1\right)\ell + \left(\frac{\Theta}{\Omega} - 1\right)\lambda^3 + 3\left(\frac{v}{\Gamma} - 1\right)\left(\frac{\Theta}{\Omega} - 1\right)\lambda \tag{B5}$$

where

$$\Theta = \rho_{wd}\left(\frac{\chi_{wd} - \chi_{ol}^s}{\chi_{ol}^l - \chi_{ol}^s}\right) \tag{B6}$$

$$\Omega = \rho_m\left(\frac{1-\chi_{ol}^l}{1-\chi_{wd}^s}\right)\left(\frac{\chi_{wd}^s - \chi_{ol}}{\chi_{ol}^l - \chi_{ol}}\right) \tag{B7}$$

$$\Gamma = \frac{3v}{2}\left(\frac{\delta}{2} + 1\right) \tag{B8}$$

We can then solve for the height of the melt layer $H(x)$ in each region using equations (13) and (14):

$$H_{MPZ}^4 = \Psi\Theta\left(\Gamma\left(\frac{x^4}{4} - \frac{x^2}{2}\right) + \frac{vx^2}{2}\right) + \aleph_0 x + \aleph_1 \tag{B9}$$

$$H_{VEZ}^4 = \Psi\Omega\left(\Gamma\left(\frac{x^4}{4} - \frac{x^2}{2}\right) + \frac{vx^2}{2}\right) + \aleph_2 x + \aleph_3 \tag{B10}$$

where

$$\Psi = \frac{48\mu}{\delta\rho g\rho_m} \tag{B11}$$

Assuming $x = 0$ is a stagnation point (the center of spreading), and applying the boundary conditions [equations (9), (10), (11), (12)] yields four equations that can be solved for the constants $\aleph_i$:

$$\left.\frac{\partial H_{MPZ}^4}{\partial x}\right|_{x=0} = 0 \Rightarrow 0 = \Psi\Theta\left(\Gamma\left(\frac{x^3}{3} - x\right) - vx\right)\Big|_{x=0} + \aleph_0 \tag{B12}$$

$$H_{VEZ}^4\big|_{x=\ell} = 0 \Rightarrow 0 = \Psi\Omega\left(\Gamma\left(\frac{\ell^4}{12} - \frac{\ell^2}{2}\right) + \frac{v\ell^2}{2}\right) + \aleph_2\ell + \aleph_3 \tag{B13}$$

$$H_{MPZ}^4\big|_{x=\lambda} - H_{VEZ}^4\big|_{x=\lambda} = 0 \Rightarrow 0 = \Psi(\Theta - \Omega)\left(\Gamma\left(\frac{\lambda^4}{12} - \frac{\lambda^2}{2}\right) + \frac{v\lambda^2}{2}\right) + (\aleph_0 - \aleph_2)\lambda + \aleph_1 - \aleph_3 \tag{B14}$$

$$\left.\frac{\partial H_{MPZ}^4}{\partial x}\right|_{x=\lambda} - \left.\frac{\partial H_{VEZ}^4}{\partial x}\right|_{x=\lambda} = 0 \Rightarrow 0 = \Psi(\Theta - \Omega)\left(\Gamma\left(\frac{\lambda^3}{3} - \lambda\right) + v\lambda\right) + (\aleph_0 - \aleph_2) \tag{B15}$$

The constants as determined for this geometry are:

$$\aleph_0 = 0 \tag{B16}$$

$$\aleph_1 = -\Psi(\Theta - \Omega) \times \left(\Gamma\left(\frac{\lambda^3\ell}{3} - \frac{\lambda^4}{4} + \frac{\lambda^2}{2} - \lambda\ell\right) + v\left(\lambda\ell - \frac{\lambda^2}{2}\right)\right) - \Psi\Omega\left(\Gamma\left(\frac{\ell^4}{12} - \frac{\ell^2}{2}\right) + \frac{v\ell^2}{2}\right) \tag{B17}$$

$$\aleph_2 = \Psi(\Theta - \Omega)\left(\Gamma\left(\frac{\lambda^3}{3} - \lambda\right) + v\lambda\right) \tag{B18}$$

$$\aleph_3 = -\Psi\Omega\left(\Gamma\left(\frac{\ell^4}{12} - \frac{\ell^2}{2}\right) + \frac{v\ell^2}{2}\right) - \ell\Psi(\Theta - \Omega)\left(\Gamma\left(\frac{\lambda^3}{3} - \lambda\right) + v\lambda\right) \tag{B19}$$

[67] **Acknowledgments.** We would like to thank L. Montesi, S. Karato, G. Richard, S. Hier-Majumder, and an anonymous reviewer for their comments on this manuscript. This work was supported under the NSF Graduate Research Fellowship and the NSF grant EAR-0330745.

References

Aharonov, E., J. A. Whitehead, P. B. Kelemen, and M. Spiegelman (1995), Channeling instability of upwelling melt in the mantle, *J. Geophys. Res.*, *100*(B10), 20,433–20,450.

Aharonov, E., M. Spiegelman, and P. B. Kelemen (1997), Three-dimensional flow and reaction in porous media: Implications for the Earth's mantle and sedimentary basins, *J. Geophys. Res.*, *102*(B7), 14,821–14,833.

Angel, R. J., D. J. Frost, N. L. Ross, and R. Hemley (2001), Stabilities and equations of state of dense hydrous magnesium silicates, *Phys. Earth Planet. Int.*, *127*, 181–196.

Bercovici, D., and S. Karato (2003), Whole mantle convection and the transition-zone water filter, *Nature*, *425*, 39–44.

Bolfan-Casanova, N., H. Keppler, and D. C. Rubie (2000), Water partitioning between nominally anhydrous minerals in the MgO-SiO_2-H_2O system up to 24 GPa: Implications for the distribution of water in the Earth's mantle, *Earth Planet. Sci. Lett.*, *182*, 209–221.

Bolfan-Casanova, N., H. Keppler, and D. C. Rubie (2003), Water partitioning at 660 km depth and evidence for very low water solubility in magnesium silicate perovskite, *Geophys. Res. Lett.*, *30*(17), 1905, doi:10.1029/2003GL017182.

Dasgupta, R., and M. M. Hirschmann (2006), Melting in the Earth's deep upper mantle caused by carbon dioxide, *Nature*, *440*, 659–662, doi:10.1038/nature04612.

Hirschmann, M., C. Aubaud, and A. C. Withers (2005), Storage capacity of H_2O in nominally anhydrous minerals in the upper mantle, *Earth Planet. Sci. Lett.*, *236*, 167–181.

Hofmann, A. W. (1997), Mantle geochemistry: The message from oceanic volcanism, *Nature*, *385*, 219–228.

Huang, X., Y. Xu, and S. Karato (2005), Water content in the transition zone from electrical conductivity of wadsleyite and ringwoodite, *Nature*, *434*, 746–749.

Huang, X., Y. Xu, and S. Karato (2006), A wet mantle conductor? (reply), *Nature*, *439*, E3–E4, doi:10.1038/nature04.

Inoue, T. (1994), Effect of water on melting phase relations and melt composition in the system Mg_2SiO_4-$MgSiO_3$-H_2O up to 15 GPa, *Phys. Earth Planet. Int.*, *85*, 237–263.

Karato, S., D. Bercovici, G. M. Leahy, G. Richard, and Z. Jing (2006), The transition-zone water filter model for global material circulation: Where do we stand?, in *Earth's Deep Water Cycle, AGU Monogr.*, vol. 168, edited by S. Jacobsen and S. Van der Lee, pp. 289–313.

Katopodes, F. V., A. M. J. Davis, and H. A. Stone (2000), Piston flow in a two-dimensional channel, *Phys. Fluids*, *12*(5), 1240–1243.

Kawamoto, T., R. L. Hervig, and J. R. Holloway (1996), Experimental evidence for a hydrous transition zone in the early Earth's mantle, *Earth Planet. Sci. Lett.*, *142*, 587–592.

Kelemen, P. B., J. A. Whitehead, E. Aharonov, and K. A. Jordahl (1995), Experiments on flow focusing in soluble porous media, with applications to melt extraction from the mantle, *J. Geophys. Res.*, *100*(B1), 475–496.

Koch, D. M., and D. L. Koch (1995), Numerical and theoretical solutions for a drop spreading below a free fluid surface, *J. Fluid Mech.*, *287*, 251–278.

Kohlstedt, D. L., H. Keppler, and D. C. Rubie (1996), Solubility of water in the α, β and γ phases of $(MgFe)_2SiO_4$, *Contrib. Mineral. Petrol.*, *123*, 345–357.

Lawrence, J. F., and M. E. Wysession (2006), Seismic evidence for subduction-transported water in the lower mantle, in *Earth's Deep Water Cycle, AGU Monogr.*, vol. 168, edited by S. Jacobsen and S. Van der Lee, p. 251.

Leahy, G. M., and D. Bercovici (2004), The influence of the transition zone water filter on convective circulation in the mantle, *Geophys. Res. Lett.*, *31*, L23605, doi:10.1029/2004GL021206.

Litasov, K., and E. Ohtani (2002), Phase relations and melt compositions in CMAS-pyrolite-H_2O system up to 25 GPa, *Phys. Earth Planet. Int.*, *134*, 105–127.

Matsukage, K. N., Z. Jing, and S. Karato (2005), Density of hydrous silicate melt at the conditions of Earth's deep upper mantle, *Nature*, *438*, 488–491, doi:10.1038/nature04.

Obayashi, M., H. Sugioka, J. Yoshimitsu, and Y. Fukao (2006), High temperature anomalies oceanward of subducting slabs at the 410-km discontinuity, *Earth Planet. Sci. Lett.*, *243*, 149–158.

Ohtani, E., Y. Nagata, A. Suzuki, and T. Kato (1995), Melting relations of peridotite and the density crossover in planetary mantles, *Chem. Geol.*, *120*, 207–221.

Ohtani, E., H. Mizobata, and H. Yurimoto (2000), Stability of dense hydrous magnesium silicate phases in the system Mg_2SiO_4-H_2O and $MgSiO_3$-H_2O at pressures up to 27 GPa, *Phys. Chem. Miner.*, *27*, 533–544.

Richard, G., M. Monnereau, and J. Ingrin (2002), Is the transition zone an empty water reservoir? Inferences from numerical model of mantle dynamics, *Earth Planet. Sci. Lett.*, *205*, 37–51.

Richard, G., D. Bercovici, and S. Karato (2006), Slab dehydration in the Earth's mantle transition zone, *Earth Planet. Sci. Lett.*, *251*, 156–167.

Richard, G., M. Monnereau, and M. Rabinowicz (2007), Slab dehydration and fluid migration at the base of the upper mantle: Implications for deep earthquake mechanisms, *Geophys. J. Int.*, *168*, 1291–1304.

Stalder, R., P. Ulmer, A. B. Thompson, and D. Günther (2001), High pressure fluids in the system MgO-SiO_2-H_2O under upper mantle conditions, *Contrib. Mineral. Petrol.*, *140*, 607–618.

Van Keken, P. E., E. H. Hauri, and C. Ballentine (2002), Mantle mixing: The generation, preservation, and destruction of chemical heterogeneity, *Annu. Rev. Earth Planet. Sci.*, *30*, 493–525.

Wang, W., and E. Takahashi (2000), Subsolidus and melting experiments of k-doped peridotite KLB-1 to 27 GPa: Its geophysical and geochemical implications, *J. Geophys. Res.*, *105*(B2), 2855–2868.

Wood, B. J. (1995), The effect of H_2O on the 410-kilometer seismic discontinuity, *Science*, *268*, 74–76.

Yoshino, T., Y. Nishihara, and S. Karato (2007), Complete wetting of olivine grain boundaries by a hydrous melt near the transition zone, *Earth Planet. Sci. Lett.*, *256*, 466–472.

Zhong, S. (1996), Analytic solutions for stokes' flow with lateral variations in viscosity, *Geophys. J. Int.*, *124*, 18–28.

D. Bercovici and G. M. Leahy, Department of Geology and Geophysics, Kline Geology Laboratory, Yale University, P.O. Box 208109, New Haven, CT 06520-8109, USA. (garrett.leahy@yale.edu)